Shaping of light beams along curves in three dimensions

José A. Rodrigo,[1,*] **Tatiana Alieva,**[1] **Eugeny Abramochkin,**[2] **and Izan Castro**[1]

[1]*Universidad Complutense de Madrid, Facultad de Ciencias Físicas, Ciudad Universitaria s/n, Madrid 28040, Spain.*

[2]*Samara branch of PN Lebedev Physical Institute, Novo-Sadovaya st. 221, Samara, 443011, Russia*

[*]*jarmar@fis.ucm.es*

Abstract: We present a method for efficient and versatile generation of beams whose intensity and phase are prescribed along arbitrary 3D curves. It comprises a non-iterative beam shaping technique that does not require solving inversion problems of light propagation. The generated beams have diffraction-limited focusing with high intensity and controlled phase gradients useful for applications such as laser micro-machining and optical trapping. Its performance and feasibility are experimentally demonstrated on several examples including multiple trapping of micron-sized particles.

OCIS codes: (140.3300) Laser beam shaping; (140.7010) Laser trapping; (090.1760) Computer holography; (090.1995) Digital holography.

References

1. M. A. Seldowitz, J. P. Allebach, and D. W. Sweeney, "Synthesis of digital holograms by direct binary search," Appl. Opt. **26**, 2788–2798 (1987).
2. V. A. Soifer, ed., *Methods for Computer Design of Diffractive Optical Elements* (Wiley, 2002).
3. G. Whyte and J. Courtial, "Experimental demonstration of holographic three-dimensional light shaping using a Gerchberg–Saxton algorithm," New J. Phys. **7**, 117 (2005).
4. T. D. Gerke and R. Piestun, "Aperiodic volume optics," Nat. Photonics **4**, 188–193 (2010).
5. Y. Roichman, B. Sun, Y. Roichman, J. Amato-Grill, and D. G. Grier, "Optical forces arising from phase gradients," Phys. Rev. Lett. **100**, 013602 (2008).
6. M. Woerdemann, C. Alpmann, M. Esseling, and C. Denz, "Advanced optical trapping by complex beam shaping," Laser Photonics Rev. 1–16 (2012).
7. M. Padgett and L. Allen, "Light with a twist in its tail," Contemp. Phys. **41**, 275–285 (2000).
8. K. Ladavac and D. Grier, "Microoptomechanical pumps assembled and driven by holographic optical vortex arrays," Opt. Express **12**, 1144–1149 (2004).
9. A. Jesacher, S. Fürhapter, C. Maurer, S. Bernet, and M. Ritsch-Marte, "Holographic optical tweezers for object manipulations at an air-liquid surface," Opt. Express **14**, 6342–6352 (2006).
10. Y. Roichman and D. G. Grier, "Three-dimensional holographic ring traps," Proc. SPIE **6483**, 64830F–5 (2007).
11. E. R. Shanblatt and D. G. Grier, "Extended and knotted optical traps in three dimensions," Opt. Express **19**, 5833–5838 (2011).
12. S.-H. Lee, Y. Roichman, and D. G. Grier, "Optical solenoid beams," Opt. Express **18**, 6988–6993 (2010).
13. E. G. Abramochkin and V. G. Volostnikov, "Spiral light beams," Physics-Uspekhi **47**, 1177–1203 (2004).
14. J. A. Rodrigo, T. Alieva, A. Cámara, O. Martínez-Matos, P. Cheben, and M. L. Calvo, "Characterization of holographically generated beams via phase retrieval based on Wigner distribution projections," Opt. Express **19**, 6064–6077 (2011).
15. S. N. S. Reihani and L. B. Oddershede, "Optimizing immersion media refractive index improves optical trapping by compensating spherical aberrations," Opt. Lett. **32**, 1998–2000 (2007).
16. W. T. M. Irvine and D. Bouwmeester, "Linked and knotted beams of light," Nat. Physics **4**, 716–720 (2008).
17. V. Garces-Chavez, D. McGloin, H. Melville, W. Sibbett, and K. Dholakia, "Simultaneous micromanipulation in multiple planes using a self-reconstructing light beam," Nat. **419**, 145–147 (2002).

#193291 - $15.00 USD Received 2 Jul 2013; revised 8 Aug 2013; accepted 8 Aug 2013; published 26 Aug 2013

18. F. Fahrbach, P. Simon, and A. Rohrbach, "Microscopy with self-reconstructing beams," Nat. Photonics **4**, 780–785 (2010).
19. J. A. Davis, D. M. Cottrell, J. Campos, M. J. Yzuel, and I. Moreno, "Encoding amplitude information onto phase-only filters," Appl. Opt. **38**, 5004–5013 (1999).

1. Introduction

Numerous techniques based on computer generated holograms have been developed to shape coherent laser beams according predesigned intensity and phase distributions. Most of them allow the generation of scalar paraxial beams with a certain complex field amplitude defined in a plane transverse to the optical axis −i.e. two-dimensional (2D) beam shaping− and require iterative algorithms for solving inversion problems of light propagation [1, 2]. Such techniques have been extended to 3D beam configurations, see for example [3, 4] and references cited therein. Nevertheless, they have demonstrated shaping only the intensity of the beam. The design of beams with a prescribed intensity and phase in 3D is a challenging problem. Inversion methods as the ones proposed in the latter works can be used for this task, but they are computationally intensive and difficult to implement. This problem becomes even more difficult if the number of constraints (e.g. transverse planes with prescribed intensity and phase distributions) is increased.

The shaping of the beam intensity and phase in 3D configurations is an attractive problem with applications in relevant research fields such as imaging, laser micro-machining and optical trapping. In particular, the generation of beams shaped along 3D curves with prescribed intensity and phase gradients is an important problem in optical trapping [5, 6]. To achieve an efficient optical trap, the beam has to be strongly focused over the sample yielding high intensity gradients (HIGs). This additional constraint increases the difficulty of the beam design. While the intensity gradients permit the trapping of the particle, the phase gradients drive it along the trap [5]. This fact has been extensively demonstrated in the case of optical vortices created by modulating Gaussian beams with a helical phase, which carry orbital angular momentum [7–9]. This type of trapping beam, however, only works when the particles are trapped against the coverslip glass, or other medium interface (see [9]). It is due to its weak axial intensity gradient which is unable to compensate the light scattering force. A *true* 3D vortex trap generated by focusing a *helical* Bessel beam was experimentally demonstrated in [10]. It consists of a ring-like trap able to move the particles around it, in the midplane of the sample. This beam has HIGs that compensate the radiation pressure, and thus can trap objects in 3D.

The design of ring-vortex traps was recently extended to other basic 3D geometry comprising rings *tilted* with respect to the focal plane, see [11]. It was obtained by solving a back-propagation problem according to the Rayleigh-Sommerfeld diffraction integral. Nevertheless, the inversion of this integral out of the paraxial domain is a cumbersome problem. Therefore, an approximation comprising a simple superposition of beam contributions −considered as infinitesimally fine threads of light associated to the target curve− was proposed in [11] to circumvent this limit. Although this is a smart strategy, the latter approximation does not warrant the correct generation of a beam with a prescribed intensity profile along arbitrary 3D curves because it neglects interference between light propagating from different regions of the curve [11]. This cross-talk in the beam can significantly degrade the shape and the intensity gradients of the light curve, and thus the performance of the optical trap.

Other important type of 3D vortex trap is the so-called *solenoid* beam that exhibits a fixed spiral shape around the optical axis [12], in which the phase gradient can be prescribed along this curve to obtain a *tractor* beam. It was achieved by imposing helical phases to a collinear superposition of Bessel beams.

In this work we develop a non-iterative technique that allows the generation of HIG beams

#193291 - $15.00 USD Received 2 Jul 2013; revised 8 Aug 2013; accepted 8 Aug 2013; published 26 Aug 2013

whose phase and intensity are prescribed along arbitrary 3D curves. This new holographic beam shaping technique is based on the formalism developed in [13] and it does not require solving an inversion problem of light propagation. We experimentally study the generation of beams shaped in distinct 3D geometries and their application for trapping of multiple micron-sized dielectric particles.

2. Principle of the technique

2.1. HIG beams shaped along 2D curves

The proposed technique is based on the theory of structurally stable coherent and monochromatic beams $F(x,y,l)$ reported in [13]. This approach, developed in the paraxial approximation, allows designing scalar beams whose intensity distribution follows a prescribed 2D curve in the $xy-$plane. The beam shape is preserved during propagation along the axial direction l except for scaling and rotation. Specifically, the complex field amplitude of a beam with Gaussian intensity profile along the curve is given, in the plane $l=0$, by the expression:

$$F\left(\mathbf{r},0\,|\,\mathbf{c}_2(t),t\in[0,T]\right)=\frac{1}{L}\int_0^T\exp\left(-\frac{[x-x_0(t)]^2+[y-y_0(t)]^2}{2w_0^2}\right)\Phi(\mathbf{r},t)\left|\mathbf{c}_2'(t)\right|\mathrm{d}t, \qquad (1)$$

where $\mathbf{r}=(x,y)$, $\mathbf{c}_2(t)=(x_0(t),y_0(t))$ is the curve in the $xy-$plane with $t\in[0,T]$, w_0 is a constant, $|\mathbf{c}_2'(t)|=\sqrt{\left[x_0'(t)\right]^2+\left[y_0'(t)\right]^2}$,

$$L=\int_0^T\left|\mathbf{c}_2'(t)\right|\mathrm{d}t \qquad (2)$$

is the length of the curve, $\mathbf{c}_2'(t)=\mathrm{d}\mathbf{c}_2/\mathrm{d}t$, and

$$\Phi(\mathbf{r},t)=\exp\left(\frac{\mathrm{i}}{w_0^2}\left[yx_0(t)-xy_0(t)\right]+\frac{\mathrm{i}\sigma}{w_0^2}\int_0^t\left[x_0(\tau)y_0'(\tau)-y_0(\tau)x_0'(\tau)\right]\mathrm{d}\tau\right), \qquad (3)$$

is a term that shapes the phase of the beam along the curve [13]. In this formalism $\sigma=1$, however, further we will use σ as a free parameter for controlling the phase gradient along the curve. Below a shorter notation $F\left(\mathbf{r}\,|\,\mathbf{c}_2\right)$ is used in cases when the curve $\mathbf{c}_2$ does not need a detailed description.

This beam shaping technique can be understood as a *light drawing tool* in the way that the function $\exp\left(-r^2/2w_0^2\right)$, where $r^2=x^2+y^2$, works as a *pencil tip* moved along the prescribed curve. These Gaussian beam terms are coherently assembled according to the trajectory $\mathbf{c}_2(t)$, where $\Phi(\mathbf{r},t)$ guarantees the phase matching in the superposition, Eq. (1). Note that beams described by a ring curve $x_0(t)+\mathrm{i}y_0(t)=R_0\exp(\mathrm{i}t)$, $t\in[0,2\pi]$, coincide with helical Laguerre-Gaussian modes of topological charge $m=R_0^2/w_0^2$, see [13], which are well-known optical vortices carrying orbital angular momentum. The vortex with opposite topological charge, $-m$, is obtained by complex conjugation: $F^*\left(\mathbf{r}\,|\,\mathbf{c}_2\right)$.

The expression Eq. (1) allows designing a structurally stable beam that preserves its shape under focusing except for rotation and scaling $\lambda\mathrm{f}/2\pi w_0^2$, being f the focal length of the lens and λ the light wavelength in the medium. Nevertheless, the Gaussian generating term does not provide high axial intensity gradient under the focusing and has to be replaced with a more appropriate one. In particular, a plane wave can be used as generating term because it is transformed into an extremely focused spot yielding both high transversal and axial intensity gradients. Therefore, the expression Eq. (1) turns into

$$G\left(\mathbf{r},0\,|\,\mathbf{c}_2(t),t\in[0,T]\right)=\frac{1}{L}\int_0^T\Phi(\mathbf{r},t)\left|\mathbf{c}_2'(t)\right|\mathrm{d}t, \qquad (4)$$

#193291 - $15.00 USD Received 2 Jul 2013; revised 8 Aug 2013; accepted 8 Aug 2013; published 26 Aug 2013

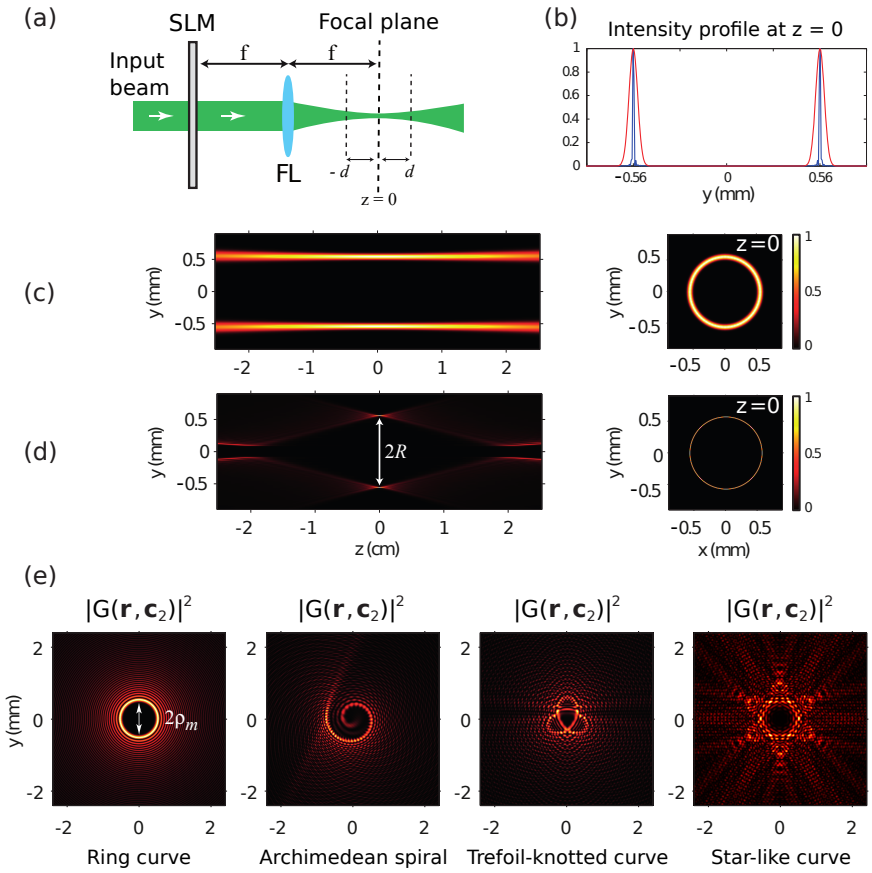

Fig. 1. (a) Setup for projecting a curve light beam in the focal region, $z \in [-d,d]$, of the focusing lens (FL). A ring-shaped beam exhibiting Gaussian and HIG intensity profiles [(b), red and blue color lines, respectively] is considered. The beam propagation in the $yz-$plane is displayed for each case, (c) and (d), correspondingly. The beam intensity at the focal plane ($z=0$) is also shown. (e) Intensity of $G(\mathbf{r}|\mathbf{c}_2)$ for several types of curves $\mathbf{c}_2$.

in order to generate a focusing beam with high intensity gradients prescribed along the curve. We underline that the plane waves $\exp\left(\mathrm{i}\left[yx_0(t)-xy_0(t)\right]/w_0^2\right)$ comprising the term $\Phi(\mathbf{r},t)$, see Eq. (3), control the position of each focused spot. While the term $\exp\left(\mathrm{i}\sigma w_0^{-2}\int_0^t\left[x_0(\tau)y_0'(\tau)-y_0(\tau)x_0'(\tau)\right]\mathrm{d}\tau\right)$ yields phase matching between the consecutive spots and thus it controls the phase gradient prescribed along the curve. Here, the parameter σ can be any real number that allows varying the phase gradient if needed. In practice, the beam is truncated by the circular aperture of the focusing lens, which is described by the circle function $\mathrm{circ}(2r/D)$ with diameter D. In this case the beam is $\mathrm{circ}(2r/D)\,G(\mathbf{r}|\mathbf{c}_2)$ and thus the *pencil tip* in the focal plane is a tiny spot of size $\delta = 2.44\lambda\,\mathrm{f}/D$ corresponding to the central maximum of the well-known Airy disc.

Before analyzing the experimental results, let us first compare the theoretically predicted focusing of the beams $F(\mathbf{r}|\mathbf{c}_2)$ and $G(\mathbf{r}|\mathbf{c}_2)$, see expressions Eq. (1) and Eq. (4) respectively. In this example we consider the ring curve $x_0(t)+\mathrm{i}y_0(t) = R_0\exp(\mathrm{i}t)$ for the generation of a vortex beam, with topological charge $m=30$ and radius $R=0.56$ mm in the focal plane, by using both methods. The setup required for the beam generation is sketched in Fig. 1(a). A

#193291 - $15.00 USD Received 2 Jul 2013; revised 8 Aug 2013; accepted 8 Aug 2013; published 26 Aug 2013

phase-only hologram that encodes the amplitude and phase of the beam is addressed into the spatial light modulator (SLM), see Methods for further details (section 5.1). In our case, the hologram is illuminated by a collimated laser beam ($\lambda = 532$ nm) and the resulting beam is then focused by a lens (FL) with focal length f $= 10$ cm. As observed in Fig. 1(b)-(d), the beam $F(\mathbf{r}\,|\,\mathbf{c}_2)$ has in the focal plane a Gaussian intensity profile [Fig. 1(b), red color line] whereas the beam $G(\mathbf{r}\,|\,\mathbf{c}_2)$ has tighter intensity profile with high transversal intensity gradient [Fig. 1(b), blue color line]. The propagation of $G(\mathbf{r}\,|\,\mathbf{c}_2)$ in the focusing region, displayed in Fig. 1(d) for the $yz-$plane, confirms the generation of high axial intensity gradient as well. In contrast, the Gaussian counterpart shown in Fig. 1(c) has low axial intensity gradient. We underline that in the case of the ring curve we recover both the Gaussian-vortex [Fig. 1(c)] and the ring-vortex [Fig. 1(d)] previously studied in [10].

Apart from the HIG condition, the beam $G(\mathbf{r}\,|\,\mathbf{c}_2)$ provides additional degrees of freedom. For instance, the topological charge m is controlled by the parameter σ without altering the radius R of the ring-vortex. In this case, $G(\mathbf{r}\,|\,\mathbf{c}_2)$ is a helical Bessel beam: $J_m(kr)\exp(\mathrm{i}m\theta)$, where $k = R_0/w_0^2 = 2\pi R/\lambda \mathrm{f}$, $J_m(kr)$ is the $m-$th order Bessel function of first kind with $m = kR_0\sigma$, and θ is the azimuthal angle, see Appendix. The opposite topological charge is obtained by changing the sign of σ. Although the radius of the ring-vortex does not depend on the topological charge, the position ρ_m of the first maximum of $J_m(kr)$ does it. Therefore, for a certain value of m the Bessel beam is significantly truncated by the lens aperture (i.e. $\mathrm{circ}(2r/D)$ pupil function). Note that this beam truncation degrades both the shape and *light efficiency* of the generated light curve. To avoid this effect and preserve the high axial intensity gradient, as the one observed in Fig. 1(d), the constraint $D \gg 2\rho_m$ has to be fulfilled. The loss of axial intensity gradient caused by increasing the topological charge was pointed out in [10] as well. We underline that a quantitative estimation of the *light efficiency* of arbitrary light curves needs further research out of the scope of this work.

To demonstrate the experimental performance of this technique, we consider different curve shapes: the latter ring curve, an Archimedean spiral, a trefoil-knotted and star-like curves. For the sake of clarity, the corresponding curve expressions are provided in Methods (section 5.2), Table 1. The intensity distributions of the resulting beams $G(\mathbf{r}\,|\,\mathbf{c}_2)$ are displayed in Fig. 1(e). As observed, these beams show a Bessel-like structure and are focused yielding the 2D light curves displayed in the first row of Fig. 2. The experimental results shown in the second row of Fig. 2 are in good agreement with the theoretical ones (first row) and clearly exhibit a HIG profile along the target curve. It is worth to mention that the exact generation of the hologram is not possible in practice and thus the generated light curve is slightly *blurred* with respect to the theoretical one. In our case the phase-only hologram is addressed into a programmable reflective LCoS-SLM (Holoeye PLUTO, 8-bit gray-level, pixel pitch of $8\,\mu$m and 1920×1080 pixels) calibrated for a 2π phase shift at the wavelength $\lambda = 532$ nm and corrected from static aberrations as reported in [14]. Although the generated beams are free of aberrations, the intensity distribution is not completely uniform along the resulting light curve due to both the limited resolution of the SLM and the non-uniformity of the input collimated laser beam. The intensity patterns obtained during the beam propagation in the focal region of the focusing lens were measured by using a sCMOS camera (Hamamatsu, Orca Flash 4.0, 16-bit gray-level, pixel size of 6.5 μm), see Methods (section 5.3), and stored as a video (Media 1).

The phase distribution of this type of beams is well-defined along curves of distinct complexity, see the third row of Fig. 2 corresponding to the theoretical phase. As we previously discussed, a ring-vortex beam has a helical phase distribution as the one shown in Fig. 2(a). The phase gradient is adapted to the curve even for more complex geometries, as the trefoil-knotted [Fig. 2(c)] and star-like [Fig. 2(d)] curves, yielding other types of vortices. In particular, the phase gradient increases in the regions of larger curvature.

#193291 - $15.00 USD Received 2 Jul 2013; revised 8 Aug 2013; accepted 8 Aug 2013; published 26 Aug 2013

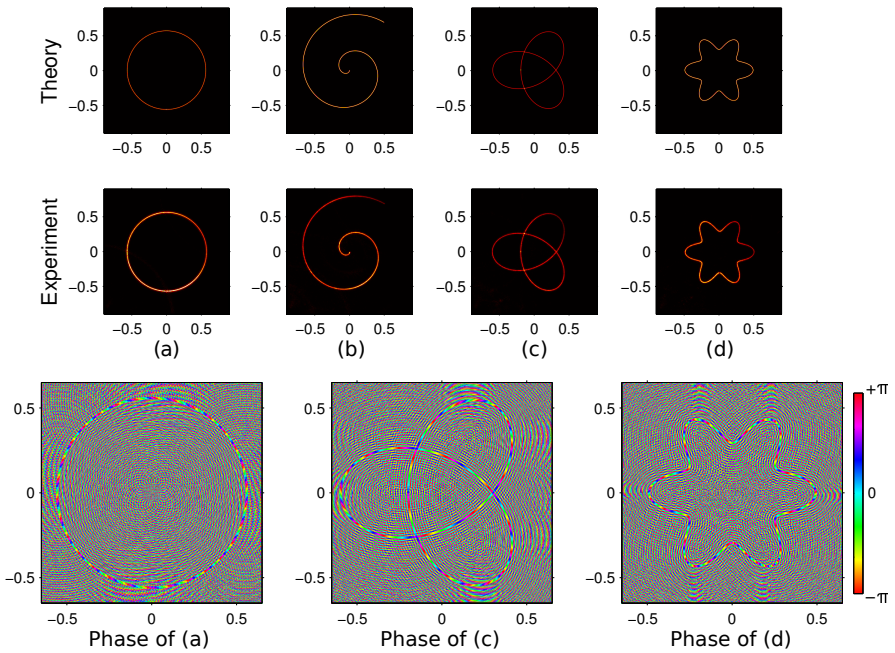

Fig. 2. (a)-(d) Intensity distribution of the beam projected in the focal plane ($z = 0$) according to several closed and open 2D curves. First and second row correspond to the expected and experimental beams. The experimental beam propagation is shown in (Media 1) for each case. Third row displays the phase of the theoretical beams shown in (a), (c) and (d). Axis units are given in mm.

2.2. HIG beams shaped along 3D curves

The described technique is well-suited for generation of HIG beams shaped into 2D curves, contained in the focal plane, and can be easily generalized to the 3D case. This is achieved by modulating each term $\Phi(\mathbf{r},t)$ with the quadratic phase function:

$$\varphi(\mathbf{r},t) = \exp\left(\mathrm{i}\pi \frac{[x-x_0(t)]^2 + [y-y_0(t)]^2}{\lambda \mathrm{f}^2} z_0(t)\right), \tag{5}$$

according to the prescribed curve $\mathbf{c}_3(t) = (x_0(t), y_0(t), z_0(t))$, where $z_0(t)$ is a *defocusing* distance defined along the curve $\mathbf{c}_2(t)$ and f is the focal length of the focusing lens. Finally, these new beam terms are coherently assembled using the expression

$$H(\mathbf{r},0\,|\,\mathbf{c}_3(t), t\in[0,T]) = \frac{1}{L}\int_0^T \varphi(\mathbf{r},t)\,\Phi(\mathbf{r},t)\,\left|\mathbf{c}_2'(t)\right|\mathrm{d}t, \tag{6}$$

which is a generalization of Eq. (4) for the 3D curve. We recall that the *pencil tip* associated with the expression Eq. (6) takes the form of a highly focused spot of diameter $\delta = 2.44\lambda \mathrm{f}/D$ in the focal region of a lens with aperture diameter D. Note that for $z_0(t) = 0$ the beam given by Eq. (6) is projected into the focal plane following the 2D curve $\mathbf{c}_2(t)$.

To demonstrate the true potential of this technique, here we study the generation of HIG beams whose intensity and phase are prescribed along 3D curves of different symmetry and complexity. Specifically, we consider a tilted ring Fig. 3(a), the Viviani's curve Fig. 3(b), an Archimedean spiral Fig. 3(c), and a trefoil-knotted curve Fig. 3(d). The corresponding curve

#193291 - $15.00 USD Received 2 Jul 2013; revised 8 Aug 2013; accepted 8 Aug 2013; published 26 Aug 2013

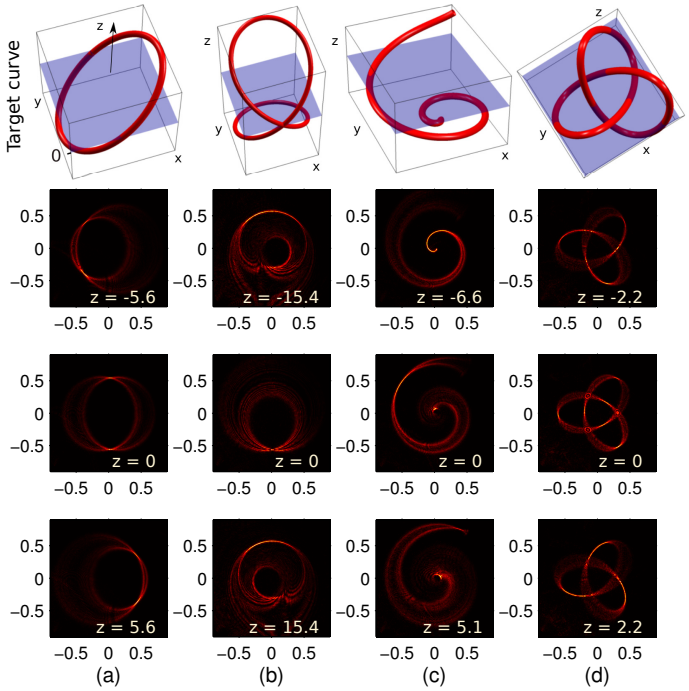

Fig. 3. Experimental results. Intensity distribution of the beams designed along 3D curves: (a) tilted ring, (b) Viviani's curve, (c) an Archimedean spiral, and a trefoil-knotted curve (d). Second, third, and fourth row display the beam propagated before, at, and after the focal plane, respectively. The overall beam prorogation was measured and stored in (Media 2) for each case. Units are given in mm.

expressions are provided in Table 1, Methods (section 5.2). These 3D structures are revealed along the beam propagation in the focal region. The beam intensity distributions measured in the focal plane ($z = 0$) are shown in the third row of Fig. 3, whereas the second and fourth row correspond to a plane before and after the focal one, respectively. For each kind of beam, the intensity distribution in the overall focusing region was also measured and stored in (Media 2). To illustrate the 3D shape of the light curve, the images stored in (Media 2) are used as 2D slices to perform the volumetric beam reconstruction displayed in Fig. 4. These results (Fig. 3 and Fig. 4) demonstrate that the HIG profile is preserved according to the 3D curve. Note that in the case of the Archimedean spiral [Fig. 3 (c) and Fig. 4(c)] the light propagating near the curve's center does not converge and diverge in the same way as the rest of the light curve. In particular, this beam present a vertical flame-like structure in the spiral's center, where the curvature is higher, as observed in the volumetric reconstruction displayed in Fig. 4(c). Moreover, the limited resolution of the hologram impedes encoding the entire beam $H(\mathbf{r}\,|\,\mathbf{c}_3)$ required to obtain high axial intensity gradient in this region of the curve. This effect is also observed in the 2D Archimedean spiral beam previously studied, see Fig. 2(b) and (Media 1).

The light curves corresponding to the Viviani's and trefoil-knotted ones are good examples of beams whose structure is interlaced in volume, and thus are difficult to generate using conventional techniques. For example, in the case of the Viviani's curve the beam $H(\mathbf{r}\,|\,\mathbf{c}_3)$ is focused into two symmetric loops (or foils) appearing on top of each other and intersecting in $z = 0$, see Fig. 3(b) and Fig. 4(b). We underline that both loops present a well-defined intensity profile without cross-talk in spite of the same light structure is generated at different propagation

#193291 - $15.00 USD Received 2 Jul 2013; revised 8 Aug 2013; accepted 8 Aug 2013; published 26 Aug 2013

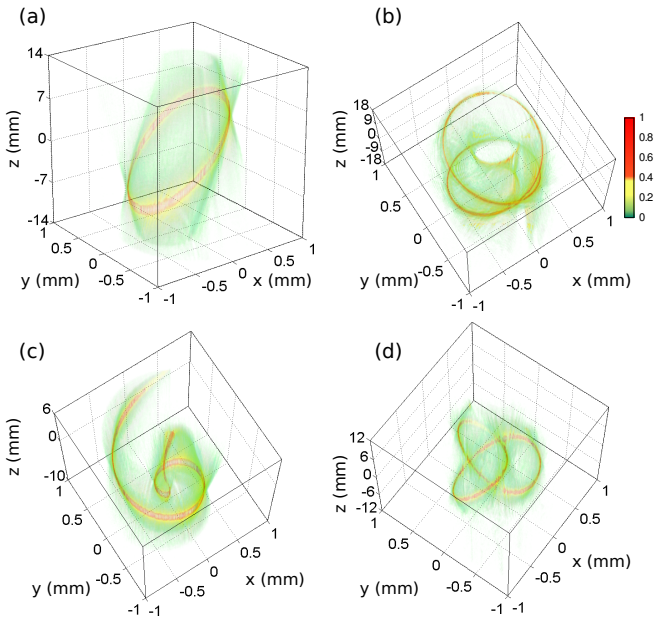

Fig. 4. Experimental results. Intensity distribution of the beams designed along 3D curves: (a) tilted ring, (b) Viviani's curve, (c) an Archimedean spiral, and a trefoil-knotted curve (d). These volumetric reconstructions were obtained from the measured beam propagations shown in (Media 2).

distances. This fact is also verified in the case of the trefoil-knotted curve, Fig. 3(d). In this case, the light propagating from a focused segment of the knot at $z < 0$ overlaps with the next segment focused for $z > 0$, see Fig. 3(d).

These results demonstrate the versatility of the developed technique for the generation of HIG beams shaped in 3D curves, even in complex geometries as the knotted one. In the next section we consider their application as optical traps and study the role played by the prescribed phase gradient.

3. Optical traps generated by beams shaped in 3D

As it has been mentioned, the complex field amplitude $H(\mathbf{r}\,|\,\mathbf{c}_3)$ is encoded into the SLM as a phase hologram. The generated beam is projected and expanded to fill the back-aperture of the microscope objective (Olympus UPLSAPO, 1.4 NA, 100×, f = 1.8 mm, $D = 5$ mm, oil immersion), which highly focuses the beam on the sample enclosed into a chamber made by attaching a glass coverslip (thickness 0.17 mm) to a standard microscope slide with double-sided tape. Our trapping setup is an inverted microscope developed by us comprising the same SLM used in the previous experiments, see Methods (section 5.4) for further details. The input laser beam (Laser Quantum, Ventus, $\lambda = 532$ nm) was collimated and expanded to illuminate the SLM display. The measured light power at the exit of the microscope objective is about 10 mW.

In Fig. 5 it is shown dielectric particles (4.7 μm diameter polystyrene sphere, Spherotech Lot. AD01, diluted in distilled water) trapped by the following beams: a ring-vortex of radius $R = 10$ μm and topological charge $m = 30$, contained in the focal plane [Fig. 5(a), Media 3] and a 14° tilted one with respect to it [Fig. 5(b), Media 4]; the Archimedean spiral extended along the optical axis [Fig. 5(c), Media 5]; and the Viviani's curve [Fig. 5(d), Media 6]. The plane

#193291 - $15.00 USD Received 2 Jul 2013; revised 8 Aug 2013; accepted 8 Aug 2013; published 26 Aug 2013

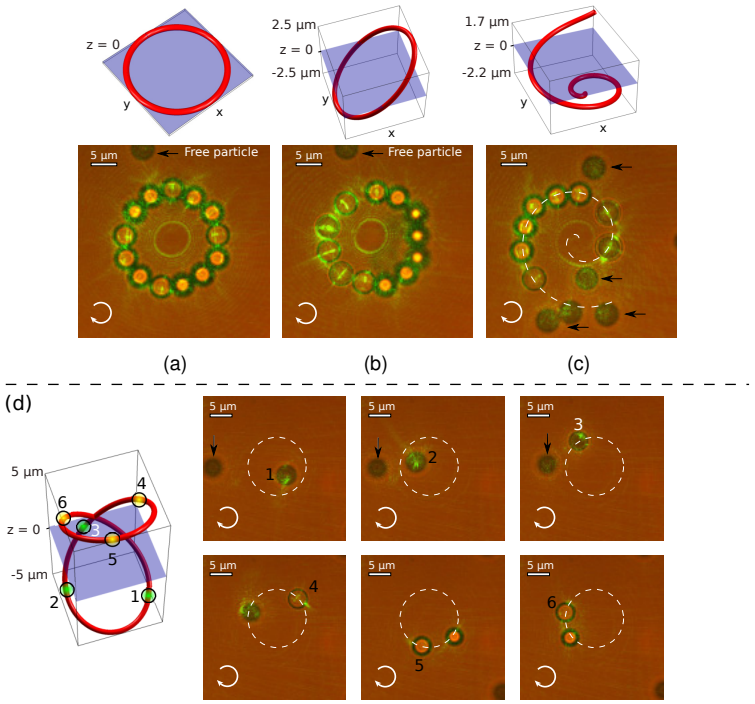

Fig. 5. Optical vortex traps shaped in different 3D configurations. The particles are trapped 10 μm in deep into the sample, black arrows indicate particles in free diffusion at the chamber bottom. The traps (a)-(d) are correspondingly shown in (Media 3, Media 4, Media 5, and Media 6).

$z = 0$ of the beam trap, see Figs. 5(a)-5(c), is 10 μm above the chamber bottom (glass coverslip). We underline that the trapping region obtained using oil immersion objectives is limited in deep due to the presence of spherical aberrations caused by the mismatch in the refractive indices of the immersion and specimen media, as reported elsewhere [15]. In our case this region is about 15 μm. To deal with this condition, in the case of Viviani's light curve (which is wider extended in the axial direction than the other considered 3D curves) the plane $z = 0$ is set at 5 μm in deep. Thus one loop *touches* the bottom surface of the chamber.

The trapped particles in the ring-vortex, Fig. 5(a), perform stable rotation around it. This rotation is also observed in the case of the tilted ring-vortex in spite of the particle goes upstream against the scattering force when passing from $z > 0$ to $z < 0$, see Fig. 5(b) and (Media 4). It is due to the phase gradient forces exerted over the particle along the curve. These results are in good agreement with the previously reported ones in [11], although the traps have been created using completely different techniques.

We recall that the direction of the particle motion can be controlled by switching the direction of the phase gradient, σ from 1 to -1, yielding clockwise and anticlockwise rotation, respectively. In the case of the Archimedean spiral the movement of the particles clearly reveals a spiral shape Fig. 5(c). For $\sigma = -1$ they perform a downstream motion towards the tail of the spiral, whereas for $\sigma = +1$ the particles move retrograde upstream along the spiral towards its center as observed in Fig. 5(c), see (Media 5).

The optical trap corresponding to the Viviani's light curve is able to move the particles in each loop comprising its shape, see Fig. 5(d). Note that the curve's projection in the $xy-$plane

#193291 - $15.00 USD Received 2 Jul 2013; revised 8 Aug 2013; accepted 8 Aug 2013; published 26 Aug 2013

is also drawn (white dashed circle) in Fig. 5(d). Specifically, the particle moves in clockwise direction along the curve according to the phase gradient. This movement starts in the position 1 in the bottom loop as depicted in Fig. 5(d), where the trapping is affected by the bottom surface of the chamber. Nevertheless, the phase gradient forces are strong enough to drive the particle to positions 2 and 3. When the particle arrives position 3, near to the loop intersection point, it keeps moving along the second loop. This loop is far enough from the glass surface yielding efficient trapping, and thus the particle motion is stable along the loop (see Media 6). The trajectory of the particle projected in the $xy-$plane, between position 3 and 6, coincides with the curve projection (white dashed circle), as expected.

4. Discussion

A simple and computationally effective technique for generation of coherent scalar beams whose intensity and phase follow prescribed open or closed 3D curves has been proposed and experimentally verified. In particular, light knotted beams in several interlaced geometries with insignificant cross-talk (undesirable interference fringes) have been experimentally generated. These results open up new perspectives for the generation of linked and knotted electromagnetic fields [16].

Although this technique is based on the paraxial framework to design the beam $H(\mathbf{r}\,|\,\mathbf{c}_3)$, Eq. (6), its properties are preserved under focusing in the nonparaxial regime yielding the target 3D light curve. Indeed, the high intensity gradients together with the phase gradients defined along the light curve permit its application as an optical trap. It has been experimentally demonstrated that micron-sized particles confined in this type of trap perform forward and backward motion to the light source according to the phase gradient. Nevertheless, further research is required for the generation of beams with a tunable phase gradient defined along the curve. This can be achieved by setting the parameter σ in Eq. (3) as a function of the curve coordinates: $\sigma = \sigma(\mathbf{c}_3(t))$.

Another important finding is that $H(\mathbf{r}\,|\,\mathbf{c}_3)$ can be understood as a Bessel-like beam extended in different geometries. For instance, $H(\mathbf{r}\,|\,\mathbf{c}_3)$ is a helical Bessel beam for the case of a ring curve. It is well-known that the Bessel beam shows self-reconstructing behavior and preserve its properties in the nonparaxial regime, which is useful in optical tweezers [17] and imaging in microscopy [18]. Therefore, this technique can be used to design self-reconstructing beams according to the standing application.

5. Methods

5.1. Holographic technique used for beam generation

A monochromatic and scalar complex field described by $A(\mathbf{r}) = a(\mathbf{r})\exp[i\phi(\mathbf{r})]$, where $a(\mathbf{r})$ and $\phi(\mathbf{r})$ are respectively the amplitude and phase distributions, can be encoded as a phase computer generated hologram (CGH) with the transmittance function

$$\Psi(\mathbf{r}) = \exp\{\mathrm{i}\psi[a(\mathbf{r}),\phi(\mathbf{r})]\}. \tag{7}$$

The encoding phase $\psi[a(\mathbf{r}),\phi(\mathbf{r})]$ can be found representing $\Psi(\mathbf{r})$ as a Fourier expansion in the domain of $\phi(\mathbf{r})$. For instance, in [19] it is demonstrated that $A(\mathbf{r})$ is recovered from the first-order term of such Fourier expansion by using $\psi[a(\mathbf{r}),\phi(\mathbf{r})] = g[a(\mathbf{r})]\,\phi(\mathbf{r})$, if the condition $\mathrm{sinc}[1-g[a(\mathbf{r})]] = a(\mathbf{r})$ is fulfilled for every value of the normalized amplitude $a(\mathbf{r}) \in [0,1]$, where $\mathrm{sinc}(t) = \sin(\pi t)/\pi t$. To isolate the encoded field $A(\mathbf{r})$ from other terms of the Fourier expansion, a fixed carrier phase $\varphi_c = 2\pi(u_0 x + v_0 y)$ is added to the latter modulation function: $\psi[a(\mathbf{r}),\phi(\mathbf{r})+\varphi_c] \bmod 2\pi$. The spatial filtering, that is performed using the 4-f telescopic system comprising the trapping setup, permits selecting the corresponding term according to the value of spatial frequencies (u_0, v_0). Further technical details are reported in [14].

#193291 - $15.00 USD Received 2 Jul 2013; revised 8 Aug 2013; accepted 8 Aug 2013; published 26 Aug 2013

5.2. *Closed and open parametric curves*

In the next table we list the parametric expressions of the curves $\mathbf{c}_3(t) = (x_0(t), y_0(t), z_0(t))$, where $t \in [0, T]$, used for generation of the beams $H(\mathbf{r}\,|\,\mathbf{c}_3)$. For all cases $T = 2\pi$ except the Archimedean spiral, where $T = 1$. The tilted ring with scaling factor $s \neq 1$ yields a tilted ellipse. Note that the 2D curves, $\mathbf{c}_2(t)$, presented in Fig. 2 are obtained using $z_0(t) = 0$.

Table 1. Parametric curves $\mathbf{c}_3(t)$

Type of curve	$x_0(t)$	$y_0(t)$	$z_0(t)$
Ring of radius R	$R\cos(t)$	$R\sin(t)$	0
Tilted ring	$R\cos(t)$	$R\sin(t)$	$sR\sin(t)$
Archimedean spiral	$-Rt\cos(10t)$	$-Rt\sin(10t)$	$sR\left(\frac{1}{2} - \sqrt{1-t^2}\right)$
Viviani's curve	$R\cos(2t)$	$R\sin(2t)$	$2sR\sin(t)$
Trefoil-knotted curve	$R[\cos(t) - 2\cos(2t)]$	$R[\sin(t) + 2\sin(2t)]$	$3sR\sin(3t)$
Star-like curve, $r(t) = 1 - \frac{1}{4}\cos(4t)$	$Rr(t)\cos(t)$	$Rr(t)\sin(t)$	0

5.3. *Measurement of the beam propagation and its volumetric reconstruction*

In the section 2.2 the propagation of the beams shaped in 3D curves is represented as a volumetric reconstruction. The measured intensity distributions are used as slices of the 3D graph shown in Fig. 4, in which a nonlinear color-map was set to help the 3D visualization. In the rest of figures (Figs. 1−3) we used a standard linear color-map to represent the 2D intensity distribution. All these intensity patterns were measured in the focal region of the focusing lens (f = 10 cm, N-BK7 glass) by using the sCMOS camera (Hamamatsu, Orca Flash 4.0) and stored as a video file in (Media 1) and (Media 2). This type of measurement is often performed by moving the digital camera in the axial direction. However, in our case the digital camera is fixed (i.e. at the focal plane of the focusing lens) and the corresponding intensity patterns are obtained by setting the proper defocussing function in the SLM. Specifically, it is achieved by encoding the modulated beam $H(\mathbf{r}\,|\,\mathbf{c}_3)\exp\left[\mathrm{i}\pi z\left(x^2+y^2\right)/\lambda \mathrm{f}^2\right]$ as the hologram given by Eq. (7), for each propagation distance z. The latter approach avoids misalignment in the measurement due to the beam propagation. In our case 251 slices were measured to obtain the volumetric reconstruction.

5.4. *Optical trapping setup*

The trapping setup sketched in Fig. 6 is an inverted microscope developed by us and comprises a reflective SLM (Holoeye PLUTO), in which the CGH is addressed. In our case the light efficiency of the SLM is about 40 %. A collimated laser beam ($\lambda = 532$ nm) is 6× expanded to illuminate the CGH. The resulting beam, $H(\mathbf{r}\,|\,\mathbf{c}_3)$, is projected to fill the back-aperture of the microscope objective (MO, Super apochromatic, Olympus, 1.4 NA, 100×), using a 1.5× Keplerian telescope comprising the relay lenses RL1 (focal length of 10 cm) and RL2 (focal length of 15 cm). A LED light source illuminates the sample, which is imaged on the CMOS color camera (Thorlabs, DCC1240C) using the tube lens (TL, focal length of 15 cm) in combination with a dichroic-mirror filter (DF) that prevents backscattered laser light from saturating the camera. A 10× Nikon objective is used as the condenser.

#193291 - $15.00 USD Received 2 Jul 2013; revised 8 Aug 2013; accepted 8 Aug 2013; published 26 Aug 2013

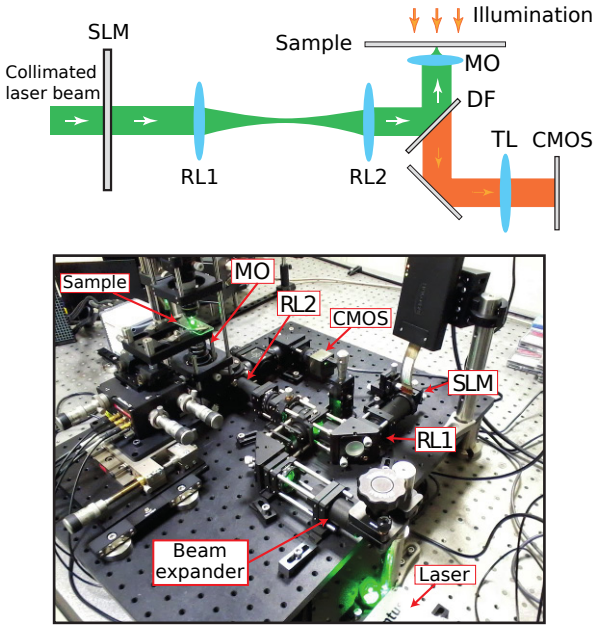

Fig. 6. Sketch of the optical trapping setup. The hologram is addressed into the SLM, which is illuminated by a collimated laser beam. The resulting beam, $H(\mathbf{r}\,|\,\mathbf{c}_3)$, is projected into the back-aperture of the microscope objective (MO), by using the relay lenses (RL1 and RL2 are set as a Keplerian telescope). A dichroic-mirror filter (DF) and the tube lens (TL) are set to image the sample on the CMOS camera.

Appendix

Here we demonstrate that in the case of a ring curve of coordinates $x_0(t) = R_0 \cos t$ and $y_0(t) = R_0 \sin t$, the beam $G(\mathbf{r}\,|\,\mathbf{c}_2)$ given by Eq. (4) corresponds to a helical Bessel one, as discussed in section 2.1. Let us consider polar coordinates $x = r\cos\theta$ and $y = r\sin\theta$. It is easy to find that the terms comprising $\Phi(\mathbf{r},t)$ are: $\exp\left(\mathrm{i}\left[yx_0(t) - xy_0(t)\right]/w_0^2\right) = \exp\left(\mathrm{i}R_0 r\sin(\theta - t)/w_0^2\right)$ and $\exp\left(\mathrm{i}\sigma w_0^{-2}\int_0^t \left[x_0(\tau)y_0'(\tau) - y_0(\tau)x_0'(\tau)\right]\mathrm{d}\tau\right) = \exp\left(\mathrm{i}R_0^2\sigma t/w_0^2\right)$. Thus, the beam is rewritten as

$$G(\mathbf{r}\,|\,\mathbf{c}_2) = \frac{1}{2\pi}\int_0^{2\pi} \exp\left(\mathrm{i}\left[\frac{\sigma R_0^2}{w_0^2}t - \frac{R_0}{w_0^2}r\sin(t-\theta)\right]\right)\mathrm{d}t. \tag{8}$$

The Bessel function is defined as

$$J_m(\rho) = \frac{1}{2\pi}\int_0^{2\pi} \exp\left(\mathrm{i}\left[mt - \rho\sin t\right]\right)\mathrm{d}t, \tag{9}$$

and therefore we finally obtain for $\sigma R_0^2/w_0^2 = m$ the expression:

$$G(\mathbf{r}\,|\,\mathbf{c}_2) = J_m\left(\frac{R_0}{w_0^2}r\right)\exp(\mathrm{i}m\theta) = J_m(kr)\exp(\mathrm{i}m\theta). \tag{10}$$

Acknowledgments

The Spanish *Ministerio de Economía y Competitividad* is acknowledged for the project TEC2011-23629.